PHYSICAL REVIEW B **86**, 014408 (2012)

Spatially resolved strain-imprinted magnetic states in an artificial multiferroic

R. V. Chopdekar,[1,*] V. K. Malik,[2] A. Fraile Rodríguez,[3] L. Le Guyader,[1] Y. Takamura,[4] A. Scholl,[5] D. Stender,[1] C. W. Schneider,[1] C. Bernhard,[2] F. Nolting,[1] and L. J. Heyderman[1]

[1]*Paul Scherrer Institute, 5232 Villigen PSI, Switzerland*

[2]*Department of Physics and Fribourg Center for Nanomaterials, University of Fribourg, 1700 Fribourg, Switzerland*

[3]*Departament de Física Fonamental and Institut de Nanociència i Nanotecnologia (IN2UB), Universitat de Barcelona, 08028 Barcelona, Spain*

[4]*Department of Chemical Engineering and Materials Science, University of California, Davis, California 95616, USA*

[5]*Advanced Light Source, Lawrence Berkeley National Laboratory, Berkeley, California 94720, USA*

(Received 22 April 2012; revised manuscript received 13 June 2012; published 10 July 2012)

Artificial multiferroic systems, in which novel properties can emerge from elastic coupling between piezoelectric and magnetostrictive phases, are a promising route to obtain significant room-temperature magnetoelectric coupling at the nanoscale. In this work, we have used element-specific soft x-ray photoemission electron microscopy to spatially resolve the effects of ferroelectric $BaTiO_3$ on the magnetic properties of ferromagnetic layers of $CoFe_2O_4$ and $NiFe_2O_4$. Resulting from the large magnetoelastic anisotropy present in these artificial multiferroic systems, a modification of the orientation and symmetry of the magnetic easy axes of the ferromagnetic film upon changing the underlying domain structure of the ferroelectric has been observed. This opens the possibility to strain-imprint magnetic states in these systems.

DOI: 10.1103/PhysRevB.86.014408 PACS number(s): 75.85.+t, 68.37.Yz, 75.70.Kw

I. INTRODUCTION

In recent years, there has been a significant increase in interest in multifunctional properties of materials both in single-phase form as well as in a variety of nanoscale composite materials for use in applications such as transducers or sensors.[1–3] Ferromagnetic-ferroelectric composites have been explored for more than thirty years, with examples ranging from $CoFe_2O_4$-$BaTiO_3$ (CFO-BTO) composites with μm-sized grains cooled from eutectic mixtures[4] to self-assembled nanocolumnar thin film heterostructures.[5]

Epitaxial thin films have exhibited large magnetoelectric interactions between ferroelectric and ferromagnetic phases.[6–8] The size of the magnetoelectric coupling depends on how well the strain is actually transmitted between the component phases and hence relies crucially on the quality of the interface. In other words, defects such as dislocations, voids, and grain boundaries have a deleterious effect on the coupling. Other important factors still not completely understood are the intermixing between the phases, the pinning of domains, the residual conductivity in the composite that may limit the strength of the applied electric field, and the influence of finite-size and surface/interface effects on the net magnetoelectric behavior.[2] Such factors can hinder the efficient electric field switching, as in the case of $CoFe_2O_4$ pillars embedded in a $BaTiO_3$ matrix where only roughly half of the pillars reorient the magnetization upon application of an electric field to the matrix.[5,9] Thus, the interactions between ferroelectric and ferromagnetic phases on the scale of individual domains is essential information for the understanding of magnetoelectric interactions in such strain-coupled composite materials.

Soft x-ray spectroscopy is well suited to observe chemical and magnetic properties of materials in an element-specific manner[10,11] and, in particular, strain effects in thin film magnetic heterostructures.[12] A spatially resolved measurement of component phases in artificial multiferroics is possible by using techniques such as x-ray photoemission electron microscopy (PEEM), which offers a powerful tool for probing both ferromagnetic order and structural or magnetic anisotropy through the use of polarization-dependent x-ray absorption at specific elemental absorption edges.[13] Using PEEM one can investigate ferroic properties of a multiferroic material such as $BiFeO_3$, which has garnered much recent attention due to its coincident room-temperature ferroelectric and antiferromagnetic properties. Magnetoelectric coupling in $BiFeO_3$-based nanostructured systems has been measured in a spatially resolved manner via both x-ray magnetic circular and magnetic linear dichroism (XMCD and XMLD) imaging,[14,15] with the so-called natural linear dichroism[16] due solely to structural sources of electronic anisotropy such as ferroelectricity also present in such systems. Additionally, low-energy electron microscopy can be used in conjunction with x-ray microscopy to study domains in such multiferroic materials.[17] However, the complex nature of the magnetic and structural interface between component phases in artificial multiferroic materials such as the interface between $BiFeO_3$ and CoFe[15] suggests that a detailed understanding of strain-mediated coupling in multiferroic interfaces is needed.

In this work, we use a combination of PEEM-based XMCD and x-ray linear dichroism (XLD) imaging to explore with high spatial resolution the strain-mediated interaction between a BTO crystalline substrate and a ferrimagnetic thin film of CFO or $NiFe_2O_4$ (NFO) grown epitaxially on the BTO crystal. We find an induced dichroism in the ferrimagnetic films grown on BTO whose origin is structural in nature, and directly corresponds to the ferroelectric domain structure of the BTO substrate. By determining the angular dependence of the linear dichroism of the film, we demonstrate that both uniaxial and biaxial strain symmetries can coexist in the same sample, which are directly linked to the orientation of the ferroelectric axis of the BTO substrate domains. At room temperature, a *c*-axis-oriented BTO domain, which has its ferroelectric axis along the surface normal, yields a fourfold symmetric strain state in the epitaxial film, whereas a neighboring *a*-axis-oriented BTO domain, whose ferroelectric axis is in the

plane of the substrate, yields a twofold symmetric strain state in the film. On changing the orientation of the ferroelectric axis of domains in the BTO substrate via temperature cycling, the magnitude and symmetry of the film strain is changed and as a result we see large changes in the magnetic anisotropy of CFO and NFO thin films. Thus we show that magnetic states can be modified via strain imprinting in an artificial multiferroic system.

II. EXPERIMENTAL METHODS

The epitaxial films measured in this work were grown on lattice matched substrates supplied by MTI Corporation using pulsed laser deposition. Sintered powder targets of single-phase spinel oxides (supplied by SurfaceNet GmbH and American Elements) were ablated using a 248 nm KrF excimer laser at a fluence of approximately 1.5 J/cm^2. Three series of samples were used to evaluate the domain structure in artificial multiferroic systems: 25 nm thick $CoFe_2O_4$ on (100)-oriented MgO and $BaTiO_3$, and 33 nm thick $NiFe_2O_4$ on (100)-oriented $BaTiO_3$ substrates. During the deposition, the substrates were maintained at an elevated temperature of 600 °C in a vacuum better than 5×10^{-6} Torr. X-ray diffraction, reflectivity, and reciprocal space mapping were performed with a Siemens D500 diffractometer to confirm the phase purity, orientation, and thickness of the films.

PEEM experiments were performed at the Surface/Interface: Microscopy (SIM) beamline[18] at the Swiss Light Source and the PEEM3 microscope of the Advanced Light Source. Samples were imaged at the Ti $L_{2,3}$ edges of BTO and the Fe $L_{2,3}$ edges of CFO and NFO films. Spectra of individual domains were taken by varying the x-ray energy and polarization as a function of sample temperature and azimuthal orientation θ with the x-ray incidence direction at a grazing angle of 16° with respect to the sample surface for the SIM microscope and 30° for the PEEM3 microscope. For both microscopes, vertically polarized x-rays have their electric field polarization axis perpendicular to the sample normal (i.e., sigma polarized).

The contrast given by XMCD is determined by the projection of magnetization $\vec{M}$ along the x-ray incidence direction $\vec{k}$ which is collinear with the x-ray photon angular momentum. We can write this relation as $I_{XMCD} \propto |\vec{M}| \cos\phi(\vec{M},\vec{k})$, and the largest contrast difference is obtained for domains with magnetization along and antiparallel to $\vec{k}$.[13] In this work, XMCD images at a specific photon energy E are obtained by taking the normalized difference between right and left circularly polarized absorption images $XMCD(E) = (I_{RCP} - I_{LCP})/(I_{RCP} + I_{LCP})$ to maximize contrast from ferromagnetic contributions and to suppress extraneous contrast originating from topographical, chemical, work function, and inhomogeneous illumination effects across the field of view.[13]

Similarly, the angular dependence of XLD contrast can be parameterized as $I_{XLD} \propto \cos^2\phi(\vec{A},\vec{E})$, with ϕ as the angle between the anisotropy axis $\vec{A}$ and the x-ray polarization vector $\vec{E}$. X-ray linear dichroism angular dependence has been fitted to this equation to determine the axis orientation in antiferromagnets such as $LaFeO_3$,[19–21] and more recently has been used to determine the axis of ferroelectric order in $Pb(Zr,Ti)O_3$.[22] Additionally, it has been found that due to symmetry constraints, the angular dependence of XMLD spectra depends on the crystal field symmetry of the sample of interest.[23] Thus, XLD can be sensitive to strain-induced changes in crystal field symmetry in artificial multiferroic systems. XLD images are obtained from the normalized difference between horizontally and vertically polarized absorption images at a given photon energy and azimuthal angle as $XLD(E,\theta) = (I_H - I_V)/(I_H + I_V)$ to emphasize contrast from ferroic order and structural anisotropy while minimizing the aforementioned extraneous contrast.

A large angular dependence on linear dichroism at the Co and Fe L edges was found in previous x-ray absorption studies of spinel thin films,[24,25] and to emphasize the angular dependence in our samples, we use the Fe L_2 XLD contrast ratio $I(\theta) = [XLD(L_{2b},\theta) - XLD(L_{2a},\theta)]/I_{\text{pre-edge}}(\theta)$. Measurements at temperatures between 260 K and 500 K were performed using the SIM microscope, whereas measurements from room temperature down to 160 K were taken using the PEEM3 microscope.

III. RESULTS AND ANALYSIS

A. Substrate-induced modification of the magnetic domain structure of spinel thin films

In order to determine the influence of the substrate-induced strain on spinel thin films, we have examined ferromagnetic domains of CFO and NFO thin films on both cubic dielectric MgO and ferroelectric BTO substrates. While macroscopic properties such as saturation magnetization and coercivity are qualitatively similar between the films, on the scale of individual domains we have found a large difference in magnetic anisotropy due to the polydomain nature of the BTO substrate.

We first compare the magnetic domain structure of demagnetized CFO films grown on (001) MgO and BTO substrates via PEEM-XMCD imaging at the Fe edge as illustrated in Fig. 1. Each of the samples were demagnetized via the following protocol: The sample was placed between the poles of an electromagnet and rotated about an in-plane [100] axis at a frequency of approximately 10 Hz while reducing the field strength from 0.8 T to zero field at 0.05 T/sec. For the PEEM-XMCD images shown in this work, the contrast is proportional to the component of magnetization projected along the x-ray incidence direction, and in this case is aligned along the horizontal axis of Fig. 1. We see that CFO films on both types of substrates show an average ferromagnetic domain size of approximately 300 nm. However, while there is no strong preference in orientation for the domains of the CFO/MgO sample, a modulation of the magnetic contrast is seen for the CFO/BTO sample whose period is on the order of 5 μm. Such a stripe modulation can be oriented either along the in-plane ⟨110⟩ or ⟨100⟩ type directions for a (001) BTO substrate, depending on the thermal history of the sample.

By taking local spectra as a function of energy and x-ray polarization in the area marked by the box in Fig. 1(b), we see that there is a large difference in absorption between horizontally and vertically polarized x-rays, and a typical set of absorption spectra and XLD is shown in Fig. 2. Fe absorption spectra of the CFO and NFO samples have similar line shapes

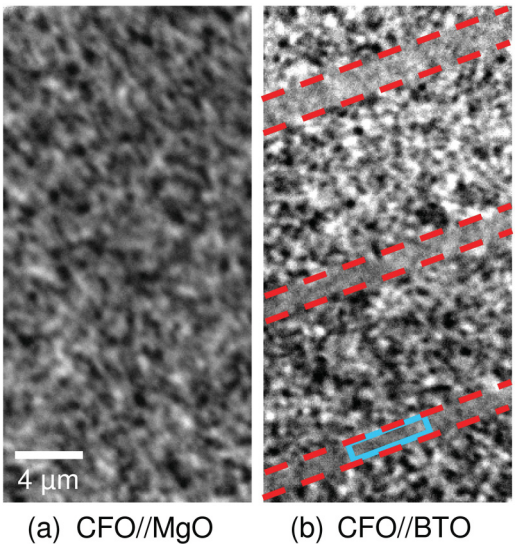

FIG. 1. (Color online) (a) Fe edge PEEM-XMCD image of CFO magnetic domain structure on MgO substrate. (b) CFO magnetic domains on BTO show a stripelike modulation of contrast whose borders are aligned along a [100] in-plane direction. Dashed lines are guides to the eye.

to spectra of Fe-containing spinels found in the literature.[24,26] Areas in which the XMCD contrast shows stripe modulation as in Fig. 1 also show a modulation of Fe L_2 XLD with the same periodicity as the XMCD modulation.

To evaluate this connection between the XMCD and XLD stripe contrast, we have measured Fe L edge XMCD and XLD domain images in the same area of a CFO/BTO sample (Fig. 3). The vector components of room-temperature magnetization in the CFO/BTO system can be measured by taking advantage of the sensitivity of the XMCD effect to the magnetization component only along the x-ray incidence direction. By rotating the sample in the microscope through seven azimuthal angles from $0^\circ \leqslant \theta \leqslant 180^\circ$, we determined the in-plane and out-of-plane magnetization components for CFO domains with a spatial resolution below 100 nm.

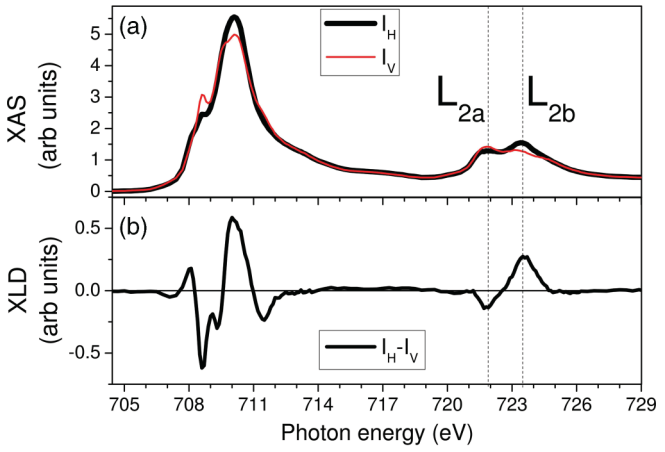

FIG. 2. (Color online) (a) X-ray absorption spectra with horizontal and vertical polarization at Fe L edge of the boxed area in Fig. 1, with (b) difference in spectra showing large dichroism at L_3 and L_2 peaks.

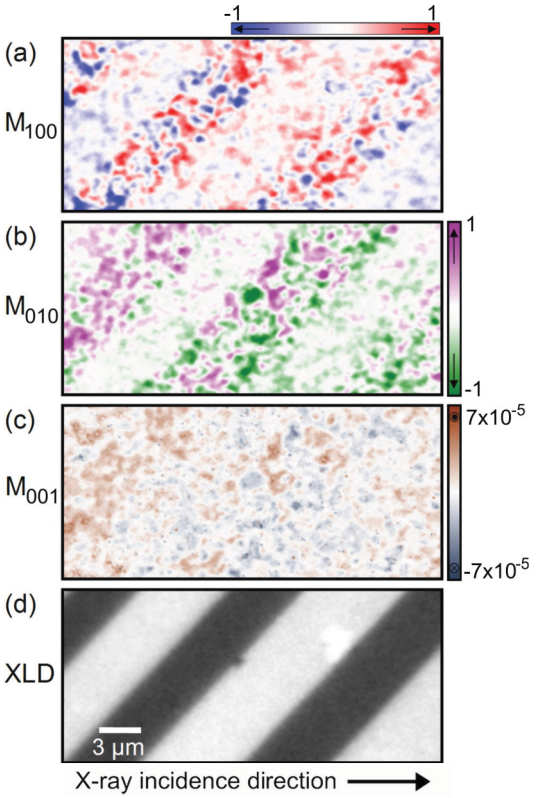

FIG. 3. (Color) Magnetization projections along in-plane (a) [100] and (b) [010] directions and (c) out-of-plane [001] direction for a (001)-oriented CFO/BTO sample, with corresponding PEEM-XLD image in panel (d), illustrating that the ferromagnetic easy axis corresponds to the film strain state as measured by XLD at the Fe L_2 edge. The direction of x-ray incidence for panel (d) is indicated by the arrow.

A color decomposition of the vector magnetization is shown in Figs. 3(a)–3(c), illustrating that the modulation of contrast is due to a strong in-plane uniaxial magnetic anisotropy in each band [Figs. 3(a) and 3(b)], with neighboring bands having anisotropy axes along orthogonal ⟨100⟩ in-plane directions and almost no out-of-plane magnetization [Fig. 3(c)]. Imaging the same area of the CFO/BTO sample using linearly polarized x-rays [Fig. 3(d)] reveals that a stripe contrast corresponds directly to the modulation in the XMCD image, showing that there is a strong signature of this modulated magnetic anisotropy visible in the XLD image.

To verify that the source of circular dichroism contrast is magnetic in origin, we have taken room-temperature images as a function of applied in-plane magnetic field via a small electromagnet coil placed underneath the sample. For this field-dependent experiment we used a NFO/BTO sample since the coercive field of NFO films was found to be much lower than that of CFO films and close to the maximum applied field from the electromagnet coil. The demagnetized NFO magnetic domain structure as seen in Fig. 4(a) is similar to that of CFO films on BTO in terms of average domain size as well as the periodic modulation of the contrast.

After negative and positive field pulses of 500 Oe shown in Figs. 4(b) and 4(c), respectively, a majority of the domains in stripe 2 orient along the field pulse direction, as seen by the

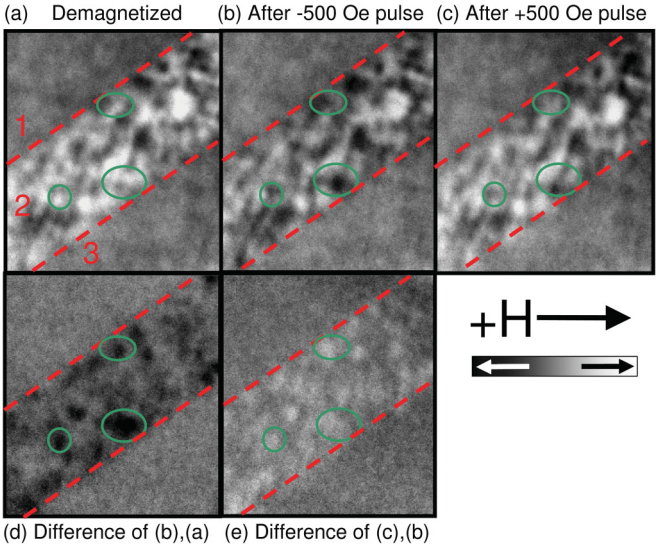

FIG. 4. (Color online) Fe edge PEEM-XMCD image of NFO/BTO in a 6 μm $\times$ 6 μm area (a) in the demagnetized state and at remanence after (b) -500 Oe and (c) $+500$ Oe field pulses. The difference images in XMCD contrast before and after (d) the negative and (e) positive field pulses indicate little contrast change in stripes 1 and 3, and a large contrast change in stripe 2. The circled regions show NFO domains which align strongly along the applied field directions.

increase in population of domains with dark contrast after the -500 Oe pulse and a subsequent increase of light domains after the $+500$ Oe pulse. However, there is no significant change in contrast for the neighboring stripes 1 and 3. To highlight this change, the demagnetized domain image was subtracted from the domain image after the -500 Oe pulse, and this difference image is shown in Fig. 4(d). The difference of the remanent XMCD image before and after the positive field pulse is shown in Fig. 4(e), confirming that the magnetization in the domains in stripe 2 can reversibly align along the applied field direction. A corresponding hysteresis loop taken in a vibrating sample magnetometer indicates that at 500 Oe the NFO/BTO sample magnetization averaged over all stripes reaches 25% of saturation. We deduce from this result that the modulation of contrast in the stripes indicates regions whose magnetic easy axis is oriented along alternating in-plane ⟨100⟩ directions of the BTO substrate.

B. Ferroelectric domain structure in $BaTiO_3$ substrates

The origin of the stripelike pattern in the CFO and NFO films shown in Figs. 1, 3, and 4 can be further elucidated by examining the BTO ferroelectric domain structure directly. Due to the insulating nature of BTO, it is difficult to image the surface ferroelectric domain structure with PEEM without a cap layer to reduce surface charging. Thus, in order to perform spectromicroscopy on a BTO substrate, we use a 3.9 nm thick $SrRuO_3$ capping layer as a conductive top electrode. The photoelectron escape depth and thus the PEEM probe depth is on the order of 5 nm,[27] so the BTO domain structure can be imaged below the thin $SrRuO_3$ layer. Figure 5(a) illustrates the XLD contrast at the Ti L_{3a} edge indicating several types of domains, and based on the contrast of XLD the types of domains at the surface of this BTO crystal are schematically shown in Fig. 5(b).

Since the growth temperature exceeds the ferroelectric Curie temperature of BTO, upon cooling the samples to room temperature the BTO substrates are polydomain in nature. As has been shown via polarized light microscopy,[28,29] the surface domain structure of polydomain BTO crystals arranges in alternating bands of domains in which either 90° or 180° domain walls separate adjacent domains. Alternating in-plane domains separated by 90° domain walls ($a1$-$a2$ type domain variants) have their walls oriented along ⟨110⟩ directions, and alternating in-plane and out-of-plane domains separated by 90° domain walls (a-c type domain variants) have walls oriented along ⟨100⟩ directions. By using linear dichroism as a contrast mechanism for BTO, one is sensitive to the axis of anisotropy in BTO and thus a difference in contrast is seen when the ferroelectric axis is along or orthogonal to

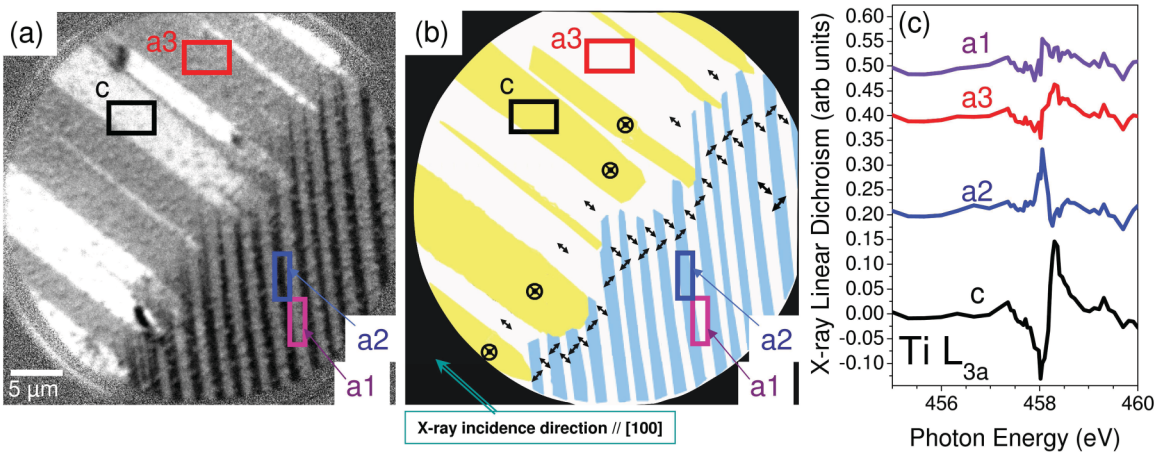

FIG. 5. (Color) (a) Ti L_{3a} edge linear dichroism image showing the different regions of a-c and $a1$-$a2$ domain variants in BTO and (b) schematic of ferroelectric axis orientation for BTO surface domains. Spectra for the different domain variants are shown in panel (c), illustrating that domains with ferroelectric axis along the x-ray incidence direction (e.g., variants $a1$ and $a3$) yield little linear dichroism, while $a2$ and c domain variants show large and opposing dichroism peaks.

the x-ray polarization. While this contrast mechanism cannot distinguish the direction of ferroelectric polarization (e.g., $c+$ and $c-$ domains would yield the same contrast), it is possible to distinguish between c and a type domains in the left half of Fig. 5(a) and to differentiate between $a1$ and $a2$ type domains in the right half of Fig. 5(a). Thus, one cannot distinguish between adjacent domains separated by 180° domain walls via PEEM-XLD, but one can see contrast between adjacent domains separated by 90° domain walls. When the Ti L edge x-rays are polarized parallel to the surface normal, a difference in absorption between in-plane and out-of-plane domains is seen whereas x-rays polarized parallel to the sample surface show a contrast between domains of different in-plane ferroelectric axis orientations.

Spectroscopy on each of these domain variants shown in Fig. 5(c) reveals that there is a dichroism at the Ti L_{3a} peak for c-axis-oriented BTO similar to that of c-axis-oriented $Pb(Zr,Ti)O_3$ thin films.[30] A clear signature of the ferroelectric axis orientation is the sign and intensity of dichroism at the lowest energy (L_{3a}) peak, with the dichroism peaks in opposing directions for c-axis-oriented domains and a-axis domains oriented perpendicular to the x-ray incidence direction. The a-axis domains whose ferroelectric axis is along the x-ray incidence direction show little linear dichroism as seen in the $a1$ and $a3$ spectra of Fig. 5(c). In other words, if the ferroelectric axis is oriented along the x-ray incidence direction, then the orbital symmetry orthogonal to the incidence direction results in the same absorption spectra for horizontally or vertically polarized x-rays, and the linear dichroism vanishes. However, if the ferroelectric axis is oriented along either the horizontal or vertical polarization axis, then the linearly polarized x-rays will be sensitive to the asymmetry in the Ti ligand field, and a linear dichroism will exist. This is the change in dichroism spectra that we can resolve in different domains [Fig. 5(c)], and can be used to spatially map the ferroelectric axis in BTO domains.

C. Angular dependence of dichroism and magnetic anisotropy in CFO

By careful measurement of the angular dependence of the Fe linear dichroism in the CFO/BTO system, we have determined the change in film strain symmetry and thus change in magnetic anisotropy in the magnetostrictive ferrimagnetic CFO film resulting from the BTO substrate domain structure. The bulk lattice mismatch between spinel ferrites ($a \approx 0.84$ nm) and $BaTiO_3$ ($a \approx 0.4$ nm) leads to compressive biaxial strain to first order in the spinel films. Due to the large magnetostriction in CFO and NFO, any structural distortion imposed by the substrate would result in a modification of the magnetic properties of the film, and this in turn results in a modification of the magnetization of the film as measured by bulk magnetometry.[7] Cubic (001)-oriented substrates yield a fourfold in-plane strain symmetry, and CFO on $SrTiO_3$ yields four easy directions along ⟨100⟩ directions.[31] Therefore, we would expect a similar strain symmetry in the paraelectric cubic phase of BTO above 410 K. At room temperature, BTO is tetragonal ($c/a \approx 1.01$) and thus a structural modulation of the fourfold strain symmetry along or perpendicular to the tetragonal axis is expected. At room temperature we can consider the film strain state as a combination of a biaxial strain induced in the CFO film due to the average lattice mismatch between bulk CFO and BTO, and an additional uniaxial strain contribution which depends on the ferroelectric domain orientation of the BTO. By changing this ferroelectric orientation, and thus modifying the film strain state, one induces changes in the ferromagnetic properties of the thin film.

As illustrated in Fig. 5, the surface domains of thermally randomized polydomain BTO will show either a mix of c- and a-axis domains or alternating bands of a-axis domains with 90° domain walls. We have measured XMCD and XLD images of CFO/BTO and NFO/BTO samples as a function of sample azimuthal angle θ with either $a1$-$a2$ mixed domains (e.g., Fig. 6) or a-c mixed domains (e.g., Fig. 7). Imaging using linearly polarized x-rays at the Fe, Co, and Ni L edges illustrates that there is strong modulation of the linear dichroism contrast in a stripelike pattern across the CFO/BTO and NFO/BTO samples. For clarity, we will only discuss the Fe L_2 edge linear dichroism angular dependence for CFO samples, though similar results for XLD spectra intensity and XLD angular dependence are found at the Co and Ni L edges. The difference in spectral magnitude but similarity in line shape between adjacent domains suggests that the adjacent film domains experience a difference in strain magnitude and/or

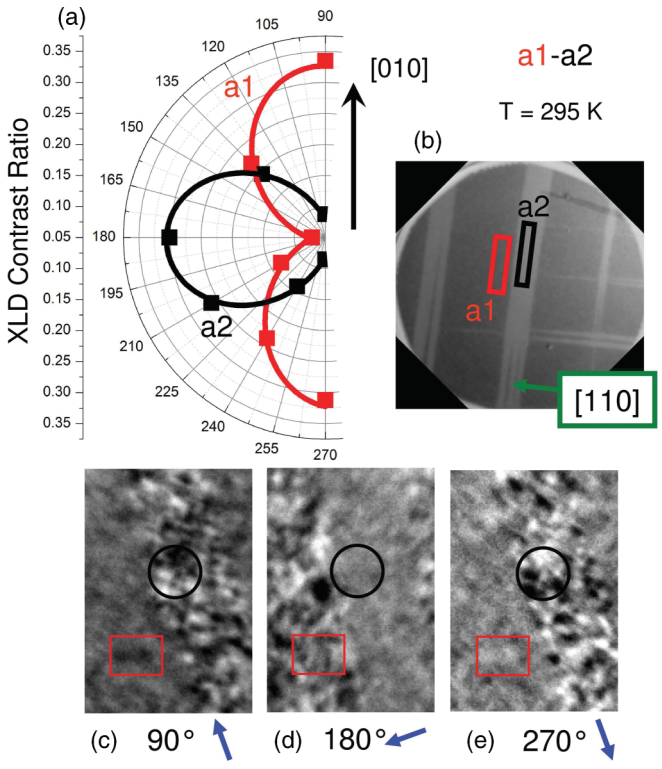

FIG. 6. (Color online) (a) Angular dependence of linear dichroism in CFO at Fe L_2 edge for $a1$-$a2$ type BTO domains at 295 K, with XLD domains in panel (b) measured at $\theta = 180°$ and arrow indicating the in-plane [110] substrate direction. (c)–(e) XMCD domains in a 7 μm × 11 μm area for $a1$ (stripe with red box) or $a2$ (stripe with black circle) domain variants for various angles θ with the x-ray incidence direction shown with small arrows, showing uniaxial in-plane magnetic anisotropy.

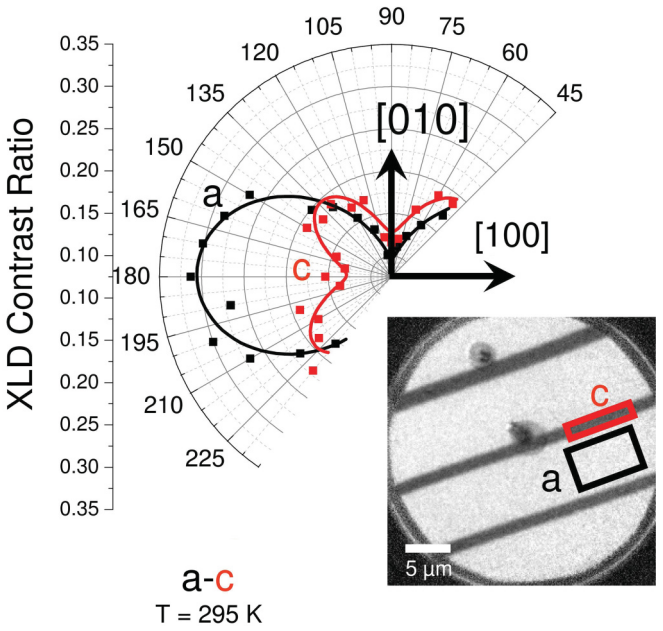

FIG. 7. (Color online) Angular dependence of linear dichroism in CFO at Fe L_2 edge for a-c type domain variants, with inset PEEM-XLD image corresponding to the area of the PEEM-XMCD image shown in Fig. 1(b). Clear differences in XLD symmetry due to the underlying BTO a-c type domain structure are seen in the azimuthal plot.

symmetry but not sign, which we hypothesize as resulting from the modulation of the CFO strain due to the reduced symmetry of the BTO unit cell. In order to confirm this hypothesis, we have measured the average CFO unit cell dimensions by reciprocal space mapping of the symmetric 004 and asymmetric 606 reflections to yield a c/a ratio of 1.0047 at room temperature for the polydomain CFO/BTO sample measured in Fig. 1(b), and a variation in room-temperature out-of plane lattice parameter of approximately 0.2% was found for repeated thermal cycling to 450 K which resulted in different populations of a- and c-axis BTO domains.

From the angular dependence of the Fe XLD we gain insight into the strain symmetry of the film resulting from the BTO substrate. The experimental XLD contrast ratios are plotted as a function of azimuthal angle θ in Figs. 6(a) and 7 and the solid lines are $\cos^2(\theta)$ fits to the data. By comparing the XLD symmetry to XMCD contrast, we directly determine how the film strain state influences the magnetic domain structure. In the XLD image in Fig. 6(b), the linear dichroism domain pattern for a region with two sets of twofold strain domains ($a1$ and $a2$) is shown, and the corresponding magnetic domain structure at the boundary between the two different strain domain variants is shown in panels (c)–(e) with the x-ray incidence direction indicated by the small arrows.

The CFO XLD domain boundaries align along the in-plane ⟨110⟩ directions, and the maximum and minimum in XLD contrast is obtained when the x-ray incidence direction is aligned along the sample ⟨100⟩ directions. In order to understand why the XLD contrast extrema are oriented along ⟨100⟩ directions, we can make a similar argument for CFO to that for the XLD of BTO surface domains in Sec. III B. In other words, for a CFO film on a BTO a-axis domain, the large lattice mismatch between CFO and BTO results in a smaller in-plane compressive distortion along the BTO ferroelectric axis and a larger compressive distortion orthogonal to it, and the XLD is at a respective minimum and maximum for those azimuthal angles. At room temperature, the BTO ferroelectric axis is along ⟨100⟩ directions, and the CFO XLD symmetry has corresponding extrema for those directions. From the XMCD images in Figs. 6(c)–6(e), we see that the $a1$-$a2$ BTO substrate domains induce a strong uniaxial magnetic anisotropy in the CFO coincident with the XLD domains, and this uniaxial magnetic anisotropy is also along the in-plane ⟨100⟩ or ⟨010⟩ axis depending on the ferroelectric orientation of the underlying BTO domain.

In Fig. 7 we measure the angular dependence of the Fe XLD contrast of CFO in an area of BTO with alternating a and c domains. One domain variant has a linear dichroism minimum at an azimuthal position $\theta = 90^\circ$ and a maximum at $\theta = 180^\circ$, which corresponds to a reduction of the compressive distortion of the Fe environment at 90° and an enhancement at 180° as discussed above. This twofold symmetry is indicative of CFO strained by an a-axis BTO domain as also seen in Fig. 6, with the longer ferroelectric axis oriented along 90° reducing the lattice mismatch between the CFO and BTO. In contrast, a fourfold symmetric strain state in the CFO film, which can be seen by linear dichroism minima at 90° and 180°, corresponds to CFO strained by a c-axis BTO domain with ferroelectric axis oriented along the surface normal.

D. Modification of CFO magnetic anisotropy and magnetic domain structure across BTO phase transitions

Making use of the tetragonal-orthorhombic and tetragonal-cubic phase transitions of the BTO substrate, we have spatially resolved the effect of different substrate domain configurations on the magnetic domain structure and strain state of CFO films. Below the cubic-tetragonal phase transition at 410 K, BTO is ferroelectric, and upon cooling below room temperature BTO undergoes a phase transition to an orthorhombic phase at 290 K and further transitions to a rhombohedral phase at 190 K. *In situ* cooling of the CFO/BTO sample in the PEEM allows us to monitor the phase-transition-dependent changes in magnetic domain configurations with XMCD imaging and also to spatially map the changes in film strain state via XLD imaging.

A dramatic difference in the CFO film domain structure can be observed by imaging the same sample area at two different temperatures with XMCD and XLD (Fig. 8). Note that while the $a1$-$a2$ type BTO domains at room temperature induce a strong magnetic contrast on the left side of Fig. 8(a) and weak contrast on the right side of (a), the contrast becomes more homogeneous in panel (b) at 260 K. There is a large difference in XLD contrast at room temperature in this area [Fig. 8(c)] whose contrast corresponds to the areas of strong and weak magnetic contrast. At 260 K, the BTO substrate is orthorhombic, and a substantial change in magnetic domain structure is accompanied by a reduction in XLD contrast between the various strain domains [Fig. 8(d)]. This reduction suggests a more homogeneous distribution of strain states in the CFO film when the BTO is in the orthorhombic phase, which results in a more homogeneous magnetic contrast at 260 K.

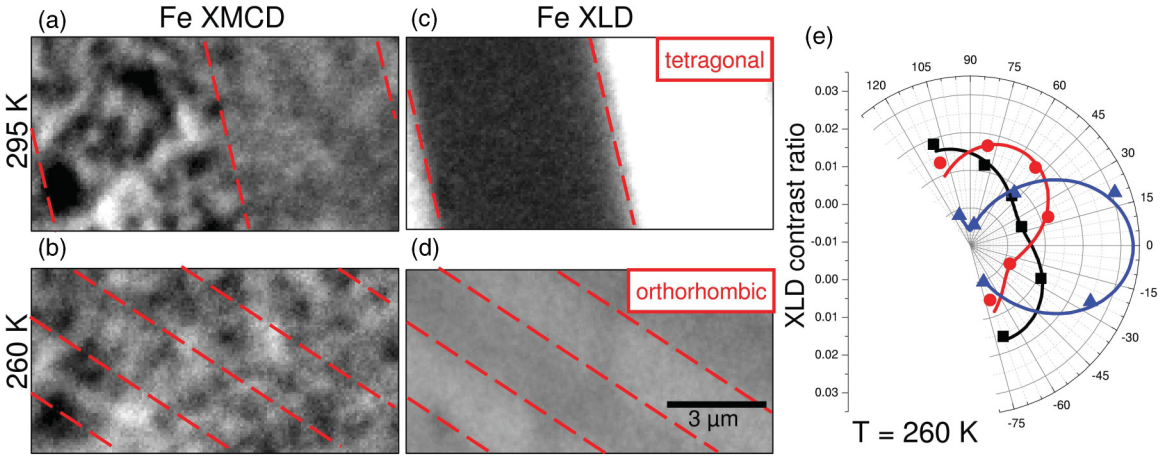

FIG. 8. (Color online) Fe L edge PEEM-XMCD images of CFO domain structure on BTO in the same area above and below the tetragonal-orthorhombic phase transition at (a) 295 K and (b) 260 K. PEEM-XLD images also taken at the same area at (c) 295 K and (d) 260 K. Contrast levels are the same between panels (a)–(b) and panels (c)–(d), and red lines are added as guides to the eye indicating strain domain boundaries. (e) Angular dependence of three different domain variants at 260 K, with $\theta = 0^\circ$ along the in-plane [100] direction at 295 K, illustrating a change in film strain symmetry due to the substrate phase transition when compared with Fig. 6(a).

In comparison to the measurements at 295 K shown in Figs. 6 and 7, the angular dependence of linear dichroism domains at 260 K in Fig. 8(e) shows that strain domains retain a uniaxial angular dependence upon cooling through the phase transition, but the number of symmetry states has changed. The ferroelectric dipole direction rotates from 6 possible ⟨100⟩ type directions at room temperature to 12 possible ⟨110⟩ type directions in the orthorhombic phase and finally to 8 possible ⟨111⟩ directions in the rhombohedral phase.[32] Upon cooling from the room-temperature tetragonal phase through the orthorhombic and rhombohedral phase transitions (Fig. 9), we see the $a1$-$a2$ CFO strain domain variants change from alternating stripes of width 1–10 μm and length of hundreds of μm, to an array of alternating parallelogram-shaped strain domains of approximate size 5 μm with one set of walls along a [100] axis and the other set at either 60° or 120° to the [100]

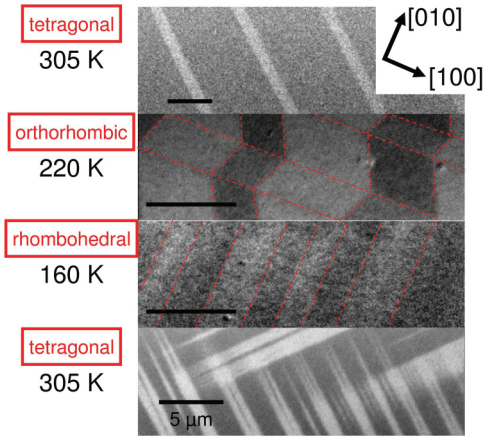

FIG. 9. (Color online) Fe edge PEEM-XLD image sequence on cooling from room temperature to 160 K and back to room temperature. Red lines are guides to the eye indicating XLD domain boundaries. The black scale bars are 5 μm long, and the black arrows indicate in-plane [100] and [010] directions.

wall. Further cooling reorients these domain walls to lie along [010] directions in the rhombohedral phase, and the $a1$-$a2$ alternating stripe pattern is restored after warming the sample back to room temperature, though the width and location of the stripes has been randomized. This change in domain wall orientation of the CFO strain domains is determined by the BTO substrate due to the necessity of having continuity of the normal component of the ferroelectric dipole across the domain wall and to minimize strain, and the zigzag pattern in the orthorhombic phase has been previously observed in BTO crystals.[33,34]

There is a strong change in the Fe XLD signal between the tetragonal and orthorhombic phases, and to verify that this change is due to a variation in strain state in the film imposed by the substrate undergoing this phase transition, we have measured the temperature-dependent XLD intensity and out-of-plane lattice parameter across the cubic-tetragonal phase transition for the same $a1$-$a2$ type domain variant CFO/BTO sample (Fig. 10). The temperature-dependent change in BTO and CFO lattice parameters is measured by variable temperature x-ray diffraction, and the 004 CFO plane spacing ($\times 4$) when passing through the tetragonal-cubic substrate transition is plotted in Fig. 10(a). For comparison, the XLD intensity at the Fe L_{2b} edge is shown for both $a1$ and $a2$ type domain variants in the same temperature region with the $a1$ ferroelectric axis oriented along the x-ray incidence direction. Upon heating through the ferroelectric Curie temperature at 410 K, the stripelike XLD domains disappear and the strong in-plane twofold ferromagnetic contrast shown in Figs. 6(c)–6(e) and 1(b) changes to a fourfold symmetric magnetic contrast similar to the CFO/MgO sample contrast seen in Fig. 1(a). Above 410 K it can be seen in Figs. 10(b) and 10(c) that the contrast for differing domains converges towards a uniform value; thus the film strain becomes homogeneous above 410 K. As mentioned earlier, in the paraelectric BTO phase, we expect the CFO film to have a cubic fourfold compressive strain, and this is reflected in the uniform linear dichroism across the sample surface. The change in domain structure measured

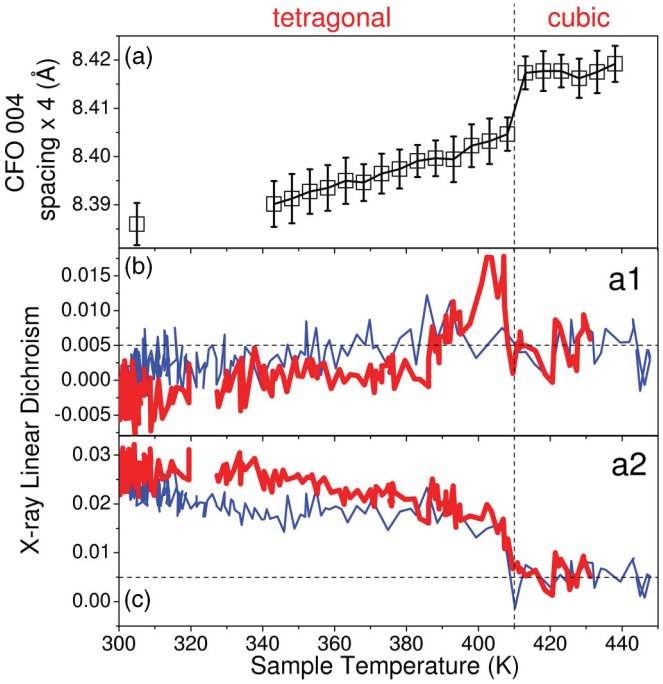

FIG. 10. (Color online) Temperature dependence of (a) out-of-plane lattice parameter and contrast for CFO/BTO linear dichroism domains with in-plane ferroelectric axis (b) along or (c) orthogonal to the x-ray incidence direction at the Fe L_{2b} edge upon warming (thick red lines) or cooling (thin blue lines) across the tetragonal-cubic BTO phase transition. Both sets of XLD domains converge towards a value of 0.005 above T_{Curie} indicating a uniform strain state in the film above 410 K.

with XMCD and XLD between 260 K and 450 K illustrates the significant influence that the substrate-induced strain has on the magnetic anisotropy of the film.

IV. CONCLUSIONS

We have simultaneously studied both nanoscale ferromagnetic and anisotropy properties of artificial multiferroic systems in the form of a ferromagnetic thin film epitaxially grown on a ferroelectric substrate. The substrate imprints a strain pattern that corresponds to the surface ferroelectric domain structure, and this structure can be modified by crossing phase transitions upon either cooling or heating the sample. As a result of the strong elastic interaction between the film and substrate, the symmetry of the film strain state, and in turn the magnetic anisotropy of the film, is strongly linked to the substrate ferroelectric state. With PEEM dichroism imaging, we have spatially mapped changes in magnetic anisotropy at the level of individual ferromagnetic domains caused by modifying the ferroelectric domain structure of the substrate. Thus, we have demonstrated the imprinting of magnetic states in an artificial multiferroic system via strain-mediated coupling at the ferroelectric-ferromagnetic interface.

ACKNOWLEDGMENTS

The authors would like to thank Anja Weber, Stefan Stutz, Georg Heldt, and Jörg Raabe. Part of this work was performed at the Swiss Light Source, Paul Scherrer Institute, Villigen, Switzerland. The Advanced Light Source is supported by the Director, Office of Science, Office of Basic Energy Sciences, of the US Department of Energy under Contract No. DE-AC02-05CH11231. This work was partially funded by EU's 7th Framework Program IFOX (NMP3-LA-2010 246102). V.K.M. and C.B. acknowledge financial support of the Swiss National Science Foundation (SNF) through Grant No. 200020-129484 and the NCCR MaNEP. A.F.R. acknowledges financial support from the Spanish MICINN through the Ramón y Cajal Programme and Grant No. MAT2009-08667, and the Catalan DIUE (Grant No. 2009SGR856).

*rajesh.chopdekar@psi.ch

[1] W. Eerenstein, N. D. Mathur, and J. F. Scott, Nature (London) **442**, 759 (2006).
[2] C.-W. Nan, M. I. Bichurin, S. Dong, D. Viehland, and G. Srinivasan, J. Appl. Phys. **103**, 031101 (2008).
[3] C. A. F. Vaz, J. Hoffman, C. H. Ahn, and R. Ramesh, Adv. Mater. **22**, 2900 (2010).
[4] J. van den Boomgaard, D. R. Terrell, R. A. J. Born, and H. F. J. I. Giller, J. Mater. Sci. **9**, 1705 (1974).
[5] H. Zheng, J. Wang, S. E. Lofland, Z. Ma, L. Mohaddes-Ardabili, T. Zhao, L. Salamanca-Riba, S. R. Shinde, S. B. Ogale, F. Bai, D. Viehland, Y. Jia, D. G. Schlom, M. Wuttig, A. Roytburd, and R. Ramesh, Science **303**, 661 (2004).
[6] M. A. Zurbuchen, T. Wu, S. Saha, J. Mitchell, and S. K. Streiffer, Appl. Phys. Lett. **87**, 232908 (2005).
[7] R. V. Chopdekar and Y. Suzuki, Appl. Phys. Lett. **89**, 182506 (2006).
[8] W. Eerenstein, M. Wiora, J. L. Prieto, J. F. Scott, and N. D. Mathur, Nat. Mater. **6**, 348 (2007).
[9] T. Zhao, A. Scholl, F. Zavaliche, H. Zheng, M. Barry, A. Doran, K. Lee, M. P. Cruz, and R. Ramesh, Appl. Phys. Lett. **90**, 123104 (2007).
[10] J. Stöhr, J. Magn. Magn. Mater. **200**, 470 (1999).
[11] T. Funk, A. Deb, S. J. George, H. Wang, and S. P. Cramer, Coordination Chemistry Reviews **249**, 3 (2005).
[12] G. van der Laan, E. Arenholz, R. V. Chopdekar, and Y. Suzuki, Phys. Rev. B **77**, 064407 (2008).
[13] A. Scholl, H. Ohldag, F. Nolting, J. Stöhr, and H. Padmore, Rev. Sci. Instrum. **73**, 1362 (2002).
[14] T. Zhao, A. Scholl, F. Zavaliche, K. Lee, M. Barry, A. Doran, M. P. Cruz, Y. H. Chu, C. Ederer, N. A. Spaldin, R. R. Das, D. M. Kim, S. H. Baek, C. B. Eom, and R. Ramesh, Nat. Mater. **5**, 823 (2006).
[15] Y.-H. Chu, L. W. Martin, M. B. Holcomb, M. Gajek, S.-J. Han, Q. He, N. Balke, C.-H. Yang, D. Lee, W. Hu, Q. Zhan, P.-L. Yang, A. Fraile Rodríguez, A. Scholl, S. X. Wang, and R. Ramesh, Nat. Mater. **7**, 478 (2008).

[16]J. Stöhr, H. A. Padmore, S. Anders, T. Stammler, and M. R. Scheinfein, Surf. Rev. Lett. **5**, 1297 (1998).
[17]S. Cherifi, R. Hertel, S. Fusil, H. Béa, K. Bouzehouane, J. Allibe, M. Bibes, and A. Barthélémy, Phys. Status Solidi Rapid Research Letters **4**, 22 (2010).
[18]U. Flechsig, F. Nolting, A. F. Rodriguez, J. Krempasky, C. Quitmann, T. Schmidt, S. Spielmann, and D. Zimoch, AIP Conf. Proc. **1234**, 319 (2010).
[19]A. Scholl, J. Stöhr, J. Lüning, J. W. Seo, J. Fompeyrine, H. Siegwart, J.-P. Locquet, F. Nolting, S. Anders, E. E. Fullerton, M. R. Scheinfein, and H. A. Padmore, Science **287**, 1014 (2000).
[20]J. Lüning, F. Nolting, A. Scholl, H. Ohldag, J. W. Seo, J. Fompeyrine, J.-P. Locquet, and J. Stöhr, Phys. Rev. B **67**, 214433 (2003).
[21]S. Czekaj, F. Nolting, L. J. Heyderman, P. R. Willmott, and G. van der Laan, Phys. Rev. B **73**, 020401 (2006).
[22]S. Polisetty, J. Zhou, J. Karthik, A. R. Damodaran, D. Chen, A. Scholl, L. W. Martin, and M. Holcomb, J. Phys.: Condens. Matter **24**, 245902 (2012).
[23]J. Kuneš and P. M. Oppeneer, Phys. Rev. B **67**, 024431 (2003).
[24]E. Arenholz, G. van der Laan, R. V. Chopdekar, and Y. Suzuki, Phys. Rev. B **74**, 094407 (2006).
[25]G. van der Laan, E. Arenholz, R. V. Chopdekar, and Y. Suzuki, Phys. Rev. B **77**, 064407 (2008).
[26]J. A. Moyer, C. A. F. Vaz, D. A. Arena, D. Kumah, E. Negusse, and V. E. Henrich, Phys. Rev. B **84**, 054447 (2011).
[27]M. Abbate, J. B. Goedkoop, F. M. F. de Groot, M. Grioni, J. C. Fuggle, S. Hofmann, H. Petersen, and M. Sacchi, Surf. Interface Anal. **18**, 65 (1992).
[28]P. W. Forsbergh, Phys. Rev. **76**, 1187 (1949).
[29]W. J. Merz, Phys. Rev. **95**, 690 (1954).
[30]E. Arenholz, G. van der Laan, A. Fraile-Rodríguez, P. Yu, Q. He, and R. Ramesh, Phys. Rev. B **82**, 140103 (2010).
[31]Y. Suzuki, G. Hu, R. B. van Dover, and R. J. Cava, J. Magn. Magn. Mater. **191**, 1 (1999).
[32]Q. Zhang, T. Cagin, and W. A. Goddard, Proc. Natl. Acad. Sci. USA **103**, 14695 (2006).
[33]D. P. Cameron, IBM J. Res. Dev. **1**, 2 (1957).
[34]M. L. Mulvmill, K. Uchino, Z. Li, and W. Cao, Philos. Mag. B **74**, 25 (1996).